# JGR Earth Surface

## RESEARCH ARTICLE

**Key Points:**

- To provide a unique combined experimental and numerical study that reveals the progress of the collisional flow erosion and transport
- To reveal that eroded basal materials are not entirely transported by the collisional granular geophysical flow
- To provide evidence for the Pareto distribution of collisional stress and its role in basal erosion and transport

**Correspondence to:**

C. E. Choi and J. Choo,
cechoi@hku.hk;
jinhyun.choo@kaist.ac.kr

# Erosion and Transport of Dry Soil Bed by Collisional Granular Flow: Insights From a Combined Experimental–Numerical Investigation

Yupeng Jiang[1,2], Pengjia Song[2] , Clarence E. Choi[2] , and Jinhyun Choo[2,3] 

[1]Institut für Baumechanik und Numerische Mechanik, Leibniz Universität Hannover, Hannover, Germany, [2]Department of Civil Engineering, The University of Hong Kong, Hong Kong, China, [3]Department of Civil and Environmental Engineering, KAIST, Daejeon, South Korea

**Abstract** Collision-induced stresses on soil beds under granular geophysical flows have been demonstrated to be highly erosive. However, it remains mostly elusive as to how a collisional granular flow erodes and transports soil bed material. This paper presents a combined experimental and numerical investigation into the mechanisms underlying collision-induced erosion and transport of dry soil beds. A series of flume experiments are conducted where collisional granular flows erode dry sand beds under varied conditions. The experiments are then back-analyzed using a hybrid continuum–discrete simulator to gain physical insight into the erosion and transport processes. Results show that the key mechanism of collision-induced erosion and transport is the retexturing of the soil bed surface. This implies that bed morphology, which has often been overlooked in mobility and hazard assessments, has profound effects on erosion and transport potential. Further, contrary to most existing models that assume all the eroded bed volume is carried away by granular flow, it is found that only up to 80% of the eroded material is transported. Also found is that the collisional stresses of the monodisperse grains in this study follow the Pareto distribution in which 80% of differences in the outcomes are due to 20% of causes. This finding suggests that there is measurable certainness in a seemingly random process of coarse grain collisions with an erodible soil bed.

**Plain Language Summary** Granular geophysical flows are among the most destructive geohazards in mountainous regions worldwide. The volume of a granular geophysical flow can increase significantly by eroding and transporting soil bed materials along its path. Understanding and modeling the mechanisms of basal erosion and transport are central to realistic hazard assessments. This study conducts a series of experiments that model collisional coarse grain flow eroding a dry sand bed. Our experiment provides insights into the quantitative relationships among the erosion profile, collisional stresses, and transported mass. The experiments are then back-analyzed using an advanced simulator to gain physical insight into the erosion and transport processes. Results reveal the key mechanism of erosion and transport induced by the collisions between the coarse grains in the flow and the erodible soil bed. This study aims to shed light on the erosion and transport dynamics of coarse granular geophysical flows.

## 1. Introduction

Granular geophysical flows are among the most destructive geohazards in mountainous regions around the globe (Cui et al., 2019; Jakob & Friele, 2009). The final deposited volume of a granular geophysical flow, as well as its destructive potential, increases with the erosion of the soil bed (Hungr et al., 2005; Iverson et al., 2011). Erosion is generally described as the shear failure of soil bed material, which occurs when the flow-induced shear stress exceeds the shear strength of the soil bed. The granular flows then transport the eroded bed materials, increasing the overall flow mass and momentum (Iverson, 2012; Iverson et al., 2011). Therefore, it is vital to understand the erosion and transport mechanism for constructing protections based on flow characteristics.

Most existing theories on soil bed erosion by geophysical flows (e.g., Iverson, 2012; Pudasaini & Krautblatter, 2021) postulate that soil bed erosion is driven mainly by frictional shear stress at the flow–bed interface. Thus, existing analytical and computational models have heavily focused on friction-induced erosion (Cao et al., 2004; McDougall & Hungr, 2005; Medina et al., 2008; Pudasaini & Krautblatter, 2021; Sovilla et al., 2006). As illustrated in Figure 1a, models of friction-induced erosion treat the soil bed and flow as two interacting homogeneous continua and equalize the transport of the eroded soil material based on continuum conservation laws.
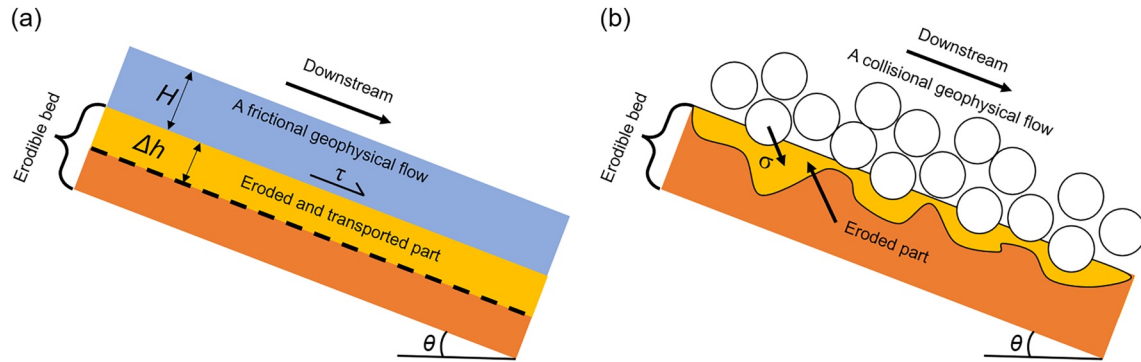
**Figure 1.** Schematic illustration of two mechanisms of erosion: (a) friction-induced erosion stress $\tau$; and (b) collision-induced erosion stress $\sigma$.

However, these types of models often overestimate the overall volume of bed transport because the erosion and transport capacity of a granular flow depend on its composition (De Haas & Woerkom, 2016; De Haas et al., 2021; Li et al., 2020), which is not explicitly considered in a continuum. Meanwhile, the erosion and transport mechanisms change with increasing flow particle size (De Haas & Woerkom, 2016; Farin et al., 2019), indicating fundamental differences between erosion and transport for coarse grain flows. Therefore, assuming that all eroded bed material is transported is unrealistic. Instead, it is necessary to distinguish between the mechanisms of bed failure, which is shear induced by friction or collision, and transport when incorporating erosion into mobility prediction tools for hazard assessment (Hungr et al., 2005; Sovilla et al., 2006). However, little to no attention has been paid to distinguish between erosion mechanisms, let alone capturing the physics that causes differences between eroded and transported volumes.

Alternatively, several field and experimental observations have suggested that the main driver of soil bed erosion is collisional boundary stress induced by coarse grains at the front of granular geophysical flow (e.g., Berger et al., 2011; De Haas & Woerkom, 2016; McArdell et al., 2007; Stock & Dietrich, 2003). See Figure 1b for a schematic illustration of collision-induced erosion. Collisional stresses dominate when the contacts between flow particles are instantaneous (Bagnold, 1954). Field observation at the Illgraben catchment, Switzerland (McArdell et al., 2007), reported that no enduring contact between flow particles is observed at the debris flow front. The existence of collisional stresses was further proven by the wear features of the force plate instrumented to monitor debris flows in the field (McCoy et al., 2013). Figure 2 shows that the wear marks on the force plate are predominantly impact marks caused by the point loads, while enduring sliding contacts between the force plate
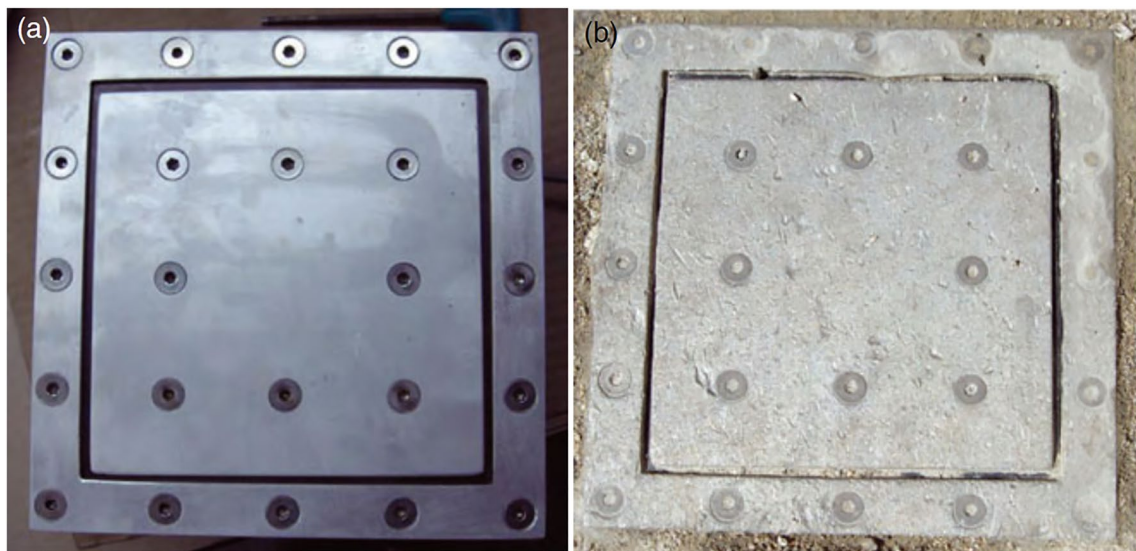


**Figure 2.** Photographs of the force plate before (a) and after (b) the monitored debris flow event (McCoy et al., 2013, figure reused by courtesy of Journal of Geophysical Research: Earth Surface).

and flow particles are not observed. Song and Choi (2021) conducted laboratory experiments to demonstrate that discrete collisional stresses induced by coarse grains on a soil bed are highly erosive. Studies have also shown that flow-seismic signals from collisional impacts of coarse particles on a soil bed can shed light on mesoscopic flow stresses and erosive potential (Roelofs et al., 2022; Zhang et al., 2021a).

Despite these observations, the mechanisms underlying collision-induced erosion and transport remain poorly understood. This lack of understanding can be attributed primarily to the difficulty of quantifying erosion and transport processes associated with collisions. Unlike friction-induced erosion, collision-induced erosion is caused by instantaneous and discrete impacts on a soil bed, making it challenging to measure the process systematically. Furthermore, due to the disparity between the sizes of grains comprising the flow and that of the soil bed, the flow and bed cannot be treated as two interacting continua as in the models of friction-induced erosion.

This work combines experiments and numerical simulations to decipher the mechanisms underlying collision-induced erosion and transport of dry soil beds. A series of flume experiments are performed whereby a dry sand bed is eroded by glass-bead flows under varied conditions. In the experiments, discrete impact loads are measured using a force plate, and kinematics are captured by a high-speed camera. These loads and kinematics data are used to calibrate a hybrid continuum–discrete simulator (Jiang et al., 2020, 2022; Zhao et al., 2023), which can simulate the extreme particle size disparity between the flow and bed materials. Using the simulator, the experiments are back-analyzed to shed light on the dynamics of soil bed erosion and transport induced by collisional geophysical granular flows.

## 2. Flume Experiments

### 2.1. Model Setup

Figure 3 shows the experimental flume used to physically model collision-induced soil bed erosion and transport. The channel is 205 mm wide and 2,650 mm long. The flume has a storage container with an inclined length of 265 mm at its upstream end to retain the initial static mass of glass beads. Just downstream from the storage container is a non-erodible bed section with a length of 1,935 mm, followed by an erodible one with a length of 450 mm. The erodible bed section is 80 mm in depth, which is designed to provide an unlimited supply of erosion (De Haas & Woerkom, 2016; Song & Choi, 2021). The grid imposed on the channel side wall has a nominal dimension of 50 mm.

### 2.2. Instrumentation

A load cell mounted underneath an acrylic plate is used to measure the collisional forces induced by a glass bead flow at a sampling rate of 2,000 Hz, which is sufficiently high for capturing the signals generated by glass bead basal collisions (Song & Choi, 2021). The plate is installed at an inclined distance of 1,450 mm downstream from the gate of the storage container. Collisional forces induced by a glass bead flow are measured to validate the computed collisional stresses (to be discussed in Section 4.2). A 3D laser scanner is used to measure the erosion depth, $\Delta h(x, y)$, on the entire surface of the erodible section by measuring the change in the depth of the erodible bed before and after each experiment. Consequently, the transported sand is considered an eroded material when calculating the average erosion depth. Only sand in the collection bin is regarded as the transported material. A high-speed camera is installed at the side of the erodible section to record the erosion and transport processes through the transparent side wall of the flume. The camera captures images with a resolution of 1,080 pixels per inch at a sampling rate of 240 frames per second.

### 2.3. Experimental Program

Soil fundamentally fails by shear, which can be induced by either enduring contact, that is, frictional shear, or instantaneous contact, that is, collisional shear, between the flow particles and the soil bed (Choi & Song, 2023; Iverson, 2012). Furthermore, scouring and mass failure are two mechanisms by which soil bed material is eroded by the shear stress exerted by debris flow (McCoy et al., 2013). Scouring occurs when the soil bed material is progressively eroded at its surface. However, mass erosion occurs when a soil bed material slides along a continuous failure plane and the soil above the failure plane is eroded en masse.

This study investigates soil bed erosion induced by collisional stresses. As such, granular flows that are collisional in nature were modeled to mimic a debris flow front. The debris flow front is well-established to be enriched with coarse particles owing to the effects of particle size segregation (Zhou et al., 2020). Furthermore, the front is poorly saturated because of the large voids between coarse grains (Berger et al., 2011; McArdell et al., 2007).
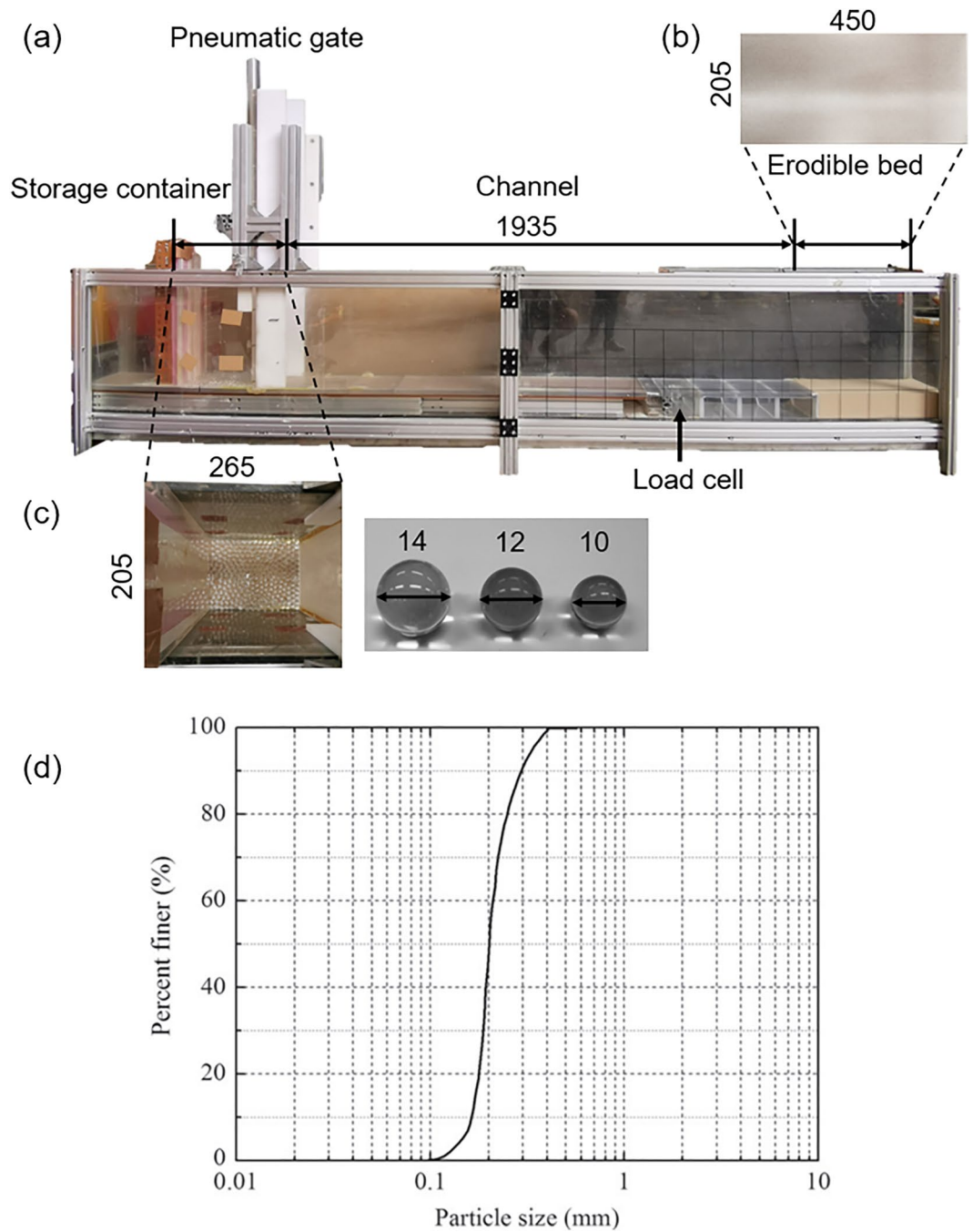
**Figure 3.** Experimental setup (all dimensions in mm): (a) side view of flume; (b) top view of erodible sand bed; (c) top view of the storage container and front view of glass beads; and (d) particle size distribution of Toyoura sand (Dong et al., 2016. Figure reused by courtesy of International Journal of Geomechanics).

Thus, collisional stresses dominate flow stresses at the debris flow front, while frictional stress and fluid stresses play a less important role (McArdell et al., 2007).

Since collisional stress is proportional to the size and velocity of a grain (Hsu et al., 2014; Song & Choi, 2021), the flume experiments are conducted under varied glass bead diameters and flume inclinations such that the soil bed is subjected to a wide range of collisional stresses. Table 1 provides the details of the experimental program. Each experiment is repeated once. The data presented in the following sections are the average of the two repeated experiments.

**Table 1**
*Experimental Program[a]*

| | |
|---|---|
| Soil density | 1,350 kg/m³ |
| Angle of repose | 32° |
| Total mass of glass beads | 2 kg |
| Particle diameter | Flume inclination |
| 10 mm | 25.0° |
| | 27.5° |
| | 30.0° |
| 12 mm | 25.0° |
| | 27.5° |
| | 30.0° |
| 14 mm | 25.0° |
| | 27.5° |
| | 30.0° |

[a]Each experiment is repeated once.

### 2.4. Consideration of Scaling

Geophysical flows in the field are typically composed of polydispersed particles. The flow particle sizes range from $10^{-5}$ to 10 m (Iverson, 1997). Consequently, debris flows in the field usually exhibit particle size segregation (Zhou et al., 2020), which is the process whereby coarse particles are transported and migrated forward to the flow front and upward to the flow surface. The segregation phenomenon causes coarse particles to be enriched at the debris flow front and flow surface. Consequently, the particles in direct contact with and erode the soil bed are finer than those that concentrate at the flow surface. In this study, slightly polydispersed flows are modeled to minimize the segregation phenomenon.

This study investigates the erosion of soil bed material by the front of a debris flow, where soil bed erosion is usually reported to occur (Berger et al., 2011). Furthermore, a debris flow front that is enriched with boulders has high void ratios and is, therefore, poorly saturated (Iverson, 1997). Field observation reported by McArdell et al. (2007) also shows that the larger boulders at the debris flow front do not have enduring contact with each other and are dominated by collisional stresses. Therefore, the fluid and frictional shear stresses are negligible at the front of debris flows.

Mesoscopic scaling was used in this study to ensure dynamic similarity between the front of a real debris flow and model flows. The dry granular flows are modeled to exclude the effects of fluid stresses on the soil bed erosion. The Savage number $N_{\text{sav}}$, which characterizes the relative importance between collisional and frictional interparticle stresses, can be used for scaling the collisional flow fronts in this study:

$$N_{\text{Sav}} = \frac{\nu_s \rho_s D_e^2 \dot{\gamma}^2}{\rho g h \cos \alpha \tan \phi'} \tag{1}$$

where $\nu_s$ is the solid volume fraction of the flow, $\rho$ is the bulk density of the flow, $D_e$ is the characteristic flow particle size, $\dot{\gamma}$ is the shear rate, $\rho_s$ is the density of the flow particles, $h$ is the flow depth, $\alpha$ is the slope and $\phi'$ is the effective friction angle of the solid grains in the flow. The numerator and the denominator of the right side of Equation 1 are the collisional stresses and the frictional shear stress within the flow, respectively. The collisional stresses dominate the flow when the Savage number $N_{\text{Sav}}$ exceeds 0.1 (Savage & Hutter, 1989). The Savage number of the model flows in this study ranges from 0.5 to 0.6, which is greater than 0.1. This shows that collisional stresses dominate the model flows and exhibit similar dynamic behavior of debris flows in the field.

Moreover, flows composed of spherical particles were modeled in this study, while the sediment particles that constitute debris flows in the field are usually angular. The interlocking between angular particles is more significant compared to that between spheres (Mirghasemi et al., 2002). The interlocking phenomenon contributes to the momentum transportation with the flow via frictional shear stress (Schofield, 2006). Thus, the debris flows in the field are more frictional compared to the modeled flows in this study.

### 2.5. Experimental Procedure

Glass beads of a mass of 2 kg are prepared in the storage container with a target bulk density of 1,600 kg/m³. The initial mass is selected to minimize the effects of glass bead deposition or bed shielding during each test (Song & Choi, 2021).

The erodible soil bed, consisting of uniform dry Toyoura sand with an angle of repose of 32°, is prepared with an initial dry density of 1,350 kg/m³. Before each test, the sand bed was carefully prepared using air pluviation (Lagioia et al., 2006). After filling the erodible section, the surface was gently flattened using a brush. In each experiment, the flume is first set to a target inclination. Then, the pneumatic actuator is used to lift the gate retaining the glass beads inside the storage container to simulate dam-break initiation. Dam-break offers a systematic and reproducible initiation process for flume experiments (Iverson, 2015). The glass beads flow down the channel and over the erodible bed.
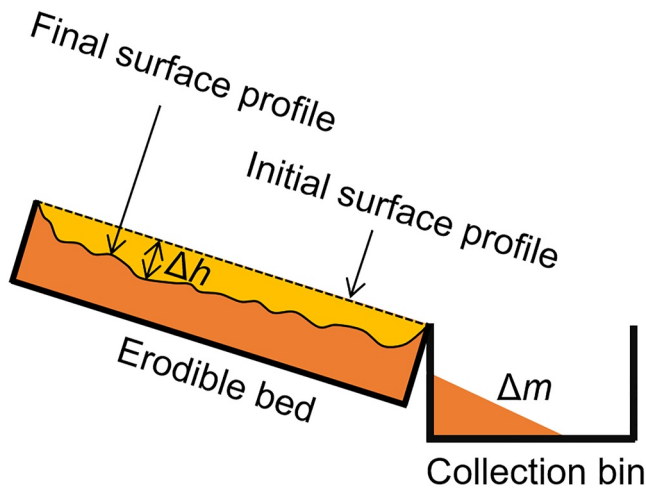
**Figure 4.** Schematic diagram showing the erosion depth, $\Delta h$, and transported mass, $\Delta m$.

It is noted that the angle of repose is 32° and the slope angle is 30° (i.e., Table 1), which together gives the factor of safety >1.0 for the clean dry sand (Lade, 2010), indicating that no surface or internal failure exists in the bed. Furthermore, a preloading procedure (to be discussed later) is used in the numerical simulations for preparing the erodible bed, ensuring no internal shear failure is induced under gravity (Jiang et al., 2022). Furthermore, the plastic strain value was measured in simulation results, which showed no signs of internal failure.

On the one hand, an increase in flow mass and particle diameter induces deeper penetration of glass beads into the erodible bed, resulting in bed shielding and deposition. On the other hand, increasing the inclination increases flow kinetic energy, which minimizes flow particles from being arrested on the bed. Based on the above considerations, the glass bead diameters and total flow mass are limited to 14 mm and 2 kg to reduce deposition, which hinders subsequent erosion measurements using a scanner on the erodible bed after each experiment. As such, a channel slope of $\theta \geq 25°$ sufficiently accelerates the flow while reducing deposition. A slope of 25° also lies within that of the field slopes. The selected experimental configuration (i.e., initial flow mass, particle diameters, and channel slope), results up to 8% of the mass of the glass beads depositing on the erodible bed for all experimental configurations. The deposited beads are mainly located near the end of the erodible bed. After each test, we carefully removed the deposited glass beads using a tweezer to measure the weight.

Figure 4 shows a schematic diagram of the erosion depth, $\Delta h$, and transported mass, $\Delta m$. Because the erosion depth varies spatiotemporally, its averaged value is used for interpretation. The experiments where glass beads are deposited on the erodible bed are picked out before laser scanning is conducted. The transported mass is obtained by sieving out the glass beads from the material in the collection bin at the end of each experiment.

## 3. Hybrid Continuum-Discrete Simulation

### 3.1. Continuum Modeling of Erodible Soil Bed

The erodible soil bed is considered a continuum because its grains are much smaller than the glass beads. Previous studies (e.g., Cui et al., 2021; Dunatunga & Kamrin, 2015; Jiang et al., 2022) have shown that dry sand subjected to dynamic impact can be well simulated by a continuum model that distinguishes among the following three states: elastic, plastic, and gasified. In this work, the elastic state is considered with Hencky elasticity, which is an extension of linear elasticity to accommodate geometric nonlinearity. The plastic state is modeled with Drucker-Prager plasticity (Drucker & Prager, 1952). Lastly, the gasified state, where the sand grains detach from each other under volumetric expansion, is simulated through a trans-phase constitutive relation (Dunatunga & Kamrin, 2015, 2017).

The trans-phase relation has been validated under a wide range of dry granular flows interacting with discrete objects (Agarwal et al., 2021; Dunatunga & Kamrin, 2017). The material point method (MPM) solver in this study simulates both shear failure induced by particle collision and gasification (Dunatunga & Kamrin, 2015). It is important to point out that the simulations in this study explicitly consider the discrete nature of coarse grain flows using the hybrid continuum-discrete solver, unlike friction-based theories, which model the flow and bed to be in constant contact.

The continuum formulation is solved numerically by the MPM, a hybrid Lagrangian-Eulerian method for largely deforming materials with history-dependent state variables. The MPM procedure consists of four stages, as depicted in Figure 5. In the first stage (Figure 5a), referred to as the particle-to-grid (P2G) transfer, the mass and momentum of the material points are mapped to nodes in the background grid. The particle–grid transfer in this work uses the general interpolation material point method, which is immune to cell-crossing noise and performs well for particle separation (Fei et al., 2021). In the second stage (Figure 5b), the nodal momentum is updated based on the discrete momentum balance equation given by

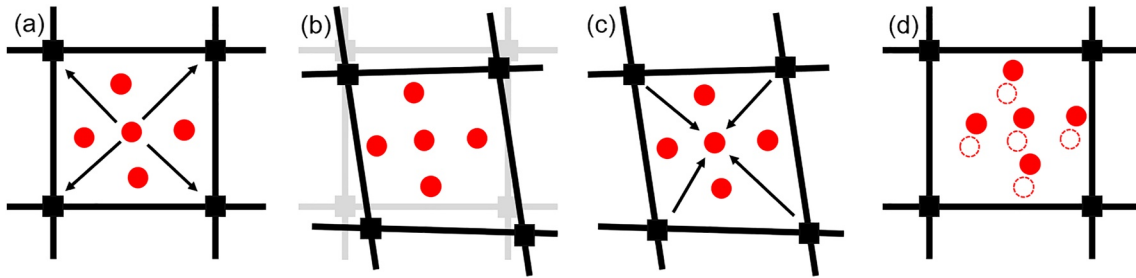$$m_i \dot{\boldsymbol{v}}_i = \boldsymbol{f}_i, \tag{2}$$

**Figure 5.** Material point method procedure: (a) particle-to-grid (P2G) transfer, (b) nodal update, (c) grid-to-particle (G2P) transfer, (d) particle update.

where subscript "$i$" denotes a nodal quantity, $m_i$ is the mass, $v_i$ is the velocity vector, and $f_i$ is the force vector, including the internal and external forces. As a standard in MPM, this work uses the explicit Euler method for the momentum update. In the third stage (Figure 5c), which is called the grid-to-particle (G2P) transfer, the updated nodal values are mapped back to the material points. The G2P transfer in this work blends the fluid-implicit-point (FLIP) method (Brackbill & Ruppel, 1986) and the particle-in-cell (PIC) method (Harlow, 1964) to balance numerical stability and energy conservation. The fourth and last stage (Figure 5d) updates the material points and proceeds to the next time step.

### 3.2. Discrete Modeling of Granular Flow

The glass beads, which are much larger than the sand grains, are modeled by the discrete element method (DEM) (Cundall & Strack, 1979). Based on Newtonian mechanics, the DEM updates the dynamics of discrete elements based on the following equations:

$$ma = f_n + f_t + g, \tag{3}$$

$$I\varphi = \mathbf{T}. \tag{4}$$

Here, $a$ and $\varphi$ are the linear and angular accelerations, respectively, $f_n$ and $f_t$ are the normal and shear contact forces, respectively, $g$ is the gravitational acceleration vector, $T$ is the torque and $m$ and $I$ are the mass and the moment of inertia of a discrete element. The discrete elements representing the flow particles are free to rotate, fall, bounce, and slide. It is noted that no significant rolling was observed during the simulated erosion process. Once the flow particles impacted the erodible bed and protrusions, the dominant modes of discrete element motion were bouncing and then falling. Through an explicit integration of these equations, the positions and velocities of the particles are updated. The contact behavior in the DEM is considered by the Hertz-Mindlin contact model, which has been validated for dry granular flows (e.g., Cagnoli & Piersanti, 2015). A normal damping coefficient was included as a purely numerical parameter to stabilize the system dynamics of DEM via energy dissipation (DEM Solutions, 2014).

### 3.3. Coupling of Continuum Soil Bed and Discrete Granular Flow

The continuum soil bed (discretized by MPM) and the discrete granular flow (modeled by DEM) are coupled through the algorithm proposed by Jiang et al. (2022). In this algorithm, each material point is assigned a radius and checked whether it is overlapped by a discrete element. If overlapped, the coupling force between the material point and the discrete element is calculated as $f_{cpl} = f n$, where $f$ is the contact magnitude related to the overlap distance $\delta$, and $n$ is the unit vector for the force direction. In this work, the contact force is calculated with the barrier method (Li et al., 2021; Zhao et al., 2022), which ensures non-penetration between material points and discrete elements. The coupling force $f_{cpl}$ is then added to both the MPM and DEM formulations. The momentum equation in the MPM, Equation 2, is modified as

$$m_i \dot{v}_i = f_i + f_{cpl}, \tag{5}$$

and Equation 3 in the DEM becomes

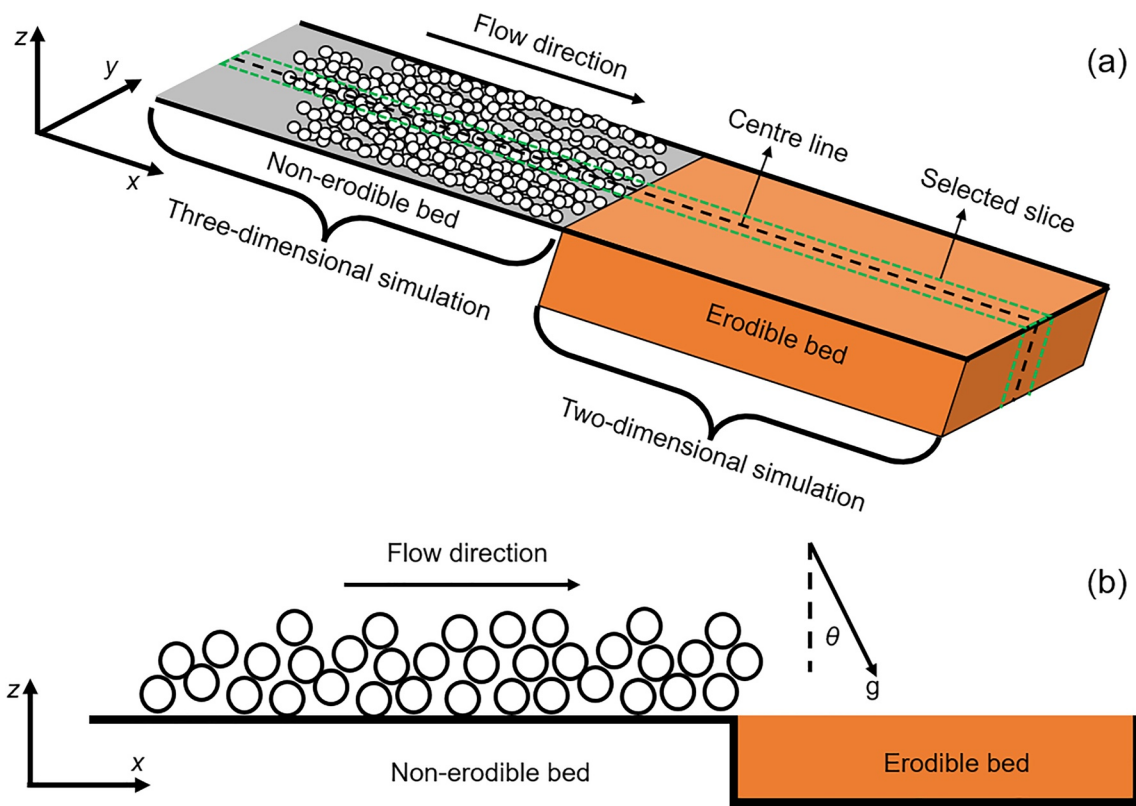$$ma = f_n + f_t + g + f_{cpl}. \tag{6}$$

**Figure 6.** Quasi-3D simulation setup: (a) full viewpoint; and (b) projected viewpoint.

Also, the P2G transfer in the MPM is modified to account for the trans-phase relation. The reader is referred to Jiang et al. (2022) for more details of the formulation and coupling algorithm.

### 3.4. Simulation Setup

The above-described formulation is used to simulate and back-analyze the flume experiments in this study. A preloading procedure was performed for the erodible bed to ensure no internal shear failure was induced under the influence of gravity (Zhao & Choo, 2020). It should be noted that the use of finer grains in the flow significantly increases the computational cost since the MPM domain needs to be discretized by a finer grid (Jiang et al., 2022). Therefore, for computational efficiency, the simulations were carried out in a quasi-3D domain, where a 3D discrete domain is coupled with a 2D hybrid domain, as illustrated in Figure 6. This approach is motivated by the work of Pasqua et al. (2022), where the computational domain of a depth-averaged method is coupled with a full 3D model through a coupling section to simulate flow-barrier impact. In this study, the glass bead flows are simulated in 3D to validate against the measured data of collisional stress over the force plate. After the flow front of the glass beads reaches the erodible bed, a slice of glass beads and dry sand bed along the centerline of the flume is simulated in 2D. As such, the coupling uses realistic collisional stress distribution as input by directly simulating the flow process before the erodible bed, which significantly improves computational efficiency.

The dimensional reduction from a full 3D model to a 2D one is achieved by defining a slice with width $d$ along the $y$-axis equal to the diameter of the flow particles, as shown in Figure 6a. Once the flow front reaches the interface between the erodible and non-erodible beds, glass beads with their centroids landing in the slice are converted to 2D discs while preserving the conservation of mass and momentum in the $z$-$x$. Figure 6b shows the schematic of the simulations after the reduction of dimensions, where the selected spheres along the central line of the 3D model are recast into discs at the lower dimensions. Other simulation parameters (e.g., contact stiffness and damping coefficients) remain unchanged as they are dimensionally independent. It helps to preserve the key dynamics (e.g., velocity and contact forces) of the glass bead flows in the $z$-$x$ plane for 2D flow-bed interaction. The erodible soil bed of material points is also discretized in 2D based on the size of the selected slice. After the

**Table 2**
*Discrete Element Method Parameters*

| Parameter | Unit | Value |
|---|---|---|
| Normal stiffness | N/m | $7.0e^{10}$ |
| Normal damping coefficient | – | 50 |
| Poisson's ratio | – | 0.2 |
| Interparticle friction coefficient | – | 0.25 |
| Particle-boundary friction coefficient | – | 0.4 |
| Density | kg/m$^3$ | 2,500 |
| Verlet distance | m | 0.02 |
| Time step | s | $1.0e^{-8}$ |

flow enters the 2D domain, the formulation couples the interaction between the glass beads and the erodible sand bed.

The lateral dimension (i.e., along the channel width) is ignored because it was assessed to be trivial compared to the overall flow dynamics. More importantly, the following conditions are observed despite ignoring the lateral dimensions: (*a*) computed contact forces and their fluctuation in the lateral direction are small and infrequent compared to that of the bed-normal direction, (*b*) computed lateral velocities and accelerations are sufficiently small compared to other velocity components (i.e., approximately 50 times smaller than that in the downstream flow direction), (*c*) particle size is sufficiently small compared to the flow width, (*d*) scanned depth of eroded surfaces (to be discussed below) in the experiments exhibited symmetry with trivial variations along the lateral direction of the channel.

### 3.5. Numerical Parameters

A structured background grid with uniformly sized (size: 1.5 mm) square cells is used for each MPM simulation. The boundaries of the container are emulated using "rigid" grids where the nodal momentum and force are zero. The MPM domain is initialized with four material points per cell. The volume of the material points ($V_p$) is calculated by dividing the total domain size by the total number of material points. A coupling radius $r_p = (V_p)^{0.5}$ and barrier stiffness of $\kappa = 1,004$ N/m are used to couple the material points and discrete elements. The mechanical parameters of the bed are assigned based on a previous study that simulated dry Toyoura sand under dynamic impacts (Jiang et al., 2022). The parameters are as follows: Young's modulus of 1 MPa, Poisson's ratio of 0.2, and the friction angle of 32°. The parameters for DEM are determined based mainly on the known properties of glass beads (Nadimi et al., 2019). However, the normal contact damping coefficient, which is unknown a priori, is calibrated by the collisional stresses measured in the flume experiments. Table 2 gives a summary of the calibrated input parameters based on the experiments. The time step size of the simulation is calculated based on the Courant–Friedrichs–Lewy (CFL) criterion, which is a necessary condition for the convergence of numerical solutions to hyperbolic partial differential equations. In practice, the CFL condition limits the time step size according to the chosen grid size (Jiang et al., 2020, 2022).

The parameters used in the DEM simulations have been calibrated against experimental data. The model parameters in the hybrid solver of MPM-DEM simulations were rigorously validated in the literature (Jiang et al., 2020, 2022). Jiang et al. (2022) reported experimental and numerical tests for rigid spheres impacting dry sand. The numerical and experimental data regarding the impact force and particle dynamics were rigorously compared. Results indicate that the MP-DEM solver simulator is physically sound and can well reproduce the complex dynamics of particle-sand interaction.

## 4. Erosion Induced by Grain Collision

### 4.1. Observed Kinematics

The collisional stresses are essentially point loads that are imposed on a small contact area between the flow particles and the soil bed (Bagnold, 1954). The contact area between the flow particles and the soil bed is discretely distributed. Therefore, collisional stresses do not create a continuous failure plane, along which the soil mass slides and erodes en masse. As such, progressive scouring of the soil bed material (McCoy et al., 2013) is the means of erosion by collisional stresses. This is consistent with experimental observations in this study.

Figure 7 shows typically observed kinematics captured by the high-speed camera mounted at the side of the flume for the glass bead flow with $D = 14$ mm and erodible dry sand bed at $\theta = 30°$. The red arrow in Figure 7a shows the flow direction. It is observed that, initially, glass beads do not significantly erode and transport sand bed material (Figure 7a). This is evident as the surface profile of the erodible bed remains uniform. At $t = 0.2$ s, glass beads are observed to impact, gasify (i.e., refer to red dashed box), and plow the sand bed material. Ensuing glass beads that impact the sand bed are impeded by protrusions formed from preceding glass bead impacts. The surface profile of the erodible bed becomes increasingly irregular with increasing discrete impacts, as shown in the red dashed box. Sand at the surface is observed to saltate and move downstream ($t = 0.4$ s). Evidently, the
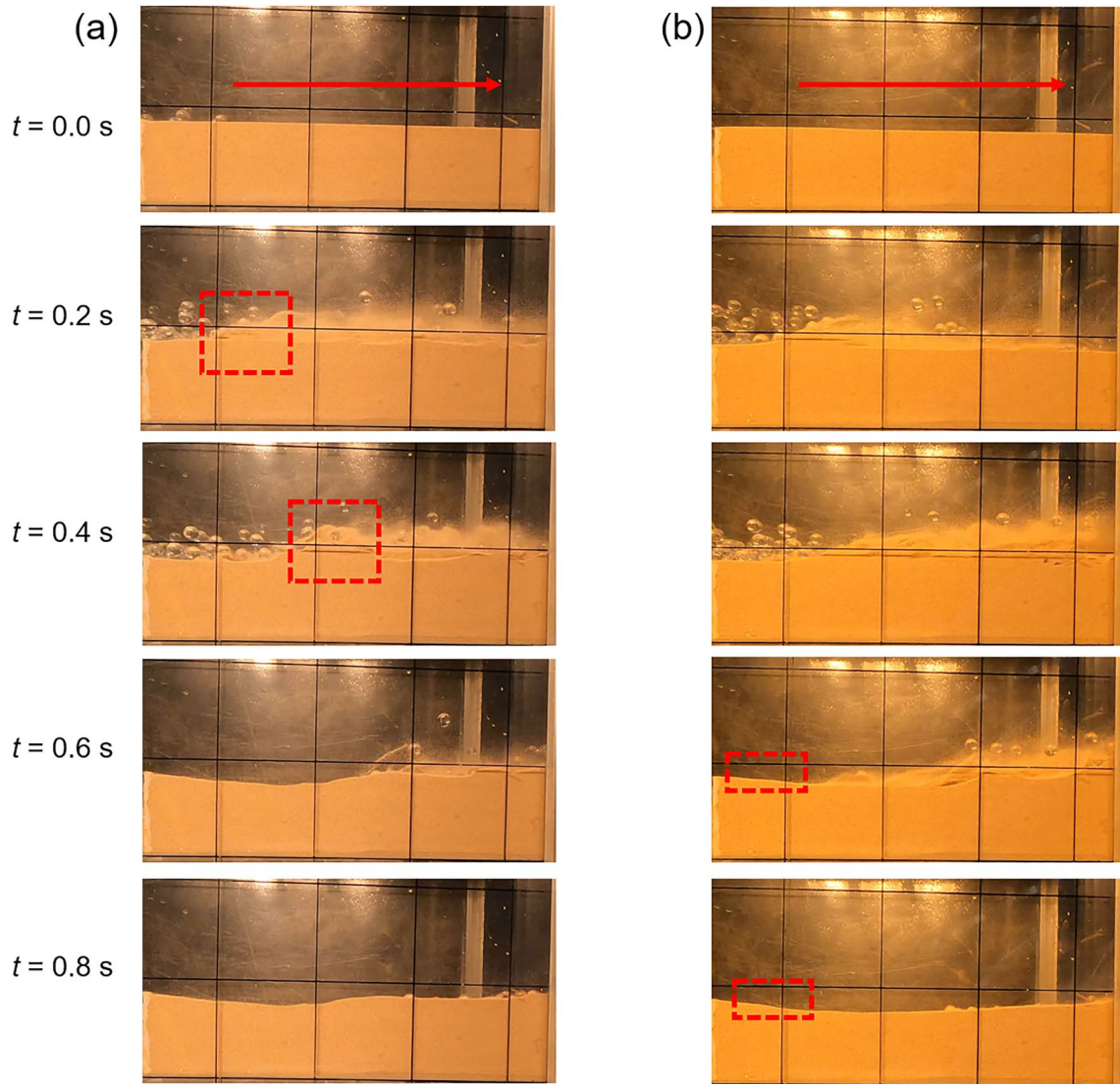
**Figure 7.** Observed kinematics of collisional glass bead flow impacting an erodible dry sand bed captured by the high-speed camera for (a) $D = 14$ mm and $\theta = 30.0°$; and (b) $D = 10$ mm and $\theta = 30.0°$. The arrow represents the flow direction; the dashed rectangles highlight the characteristic features of erosion and transportation in each time frame.

observed complex bed failure and transport processes are far from that idealized in pure continuum models based on friction-induced erosion (Medina et al., 2008; Pudasaini & Krautblatter, 2021). For the cases shown, collisions between the glass bead flows and dry sand bed are no longer evident from $t = 0.6$–0.8 s. Most of the glass bead flow has passed the erodible bed during this period. However, some parts of the sand bed, shown in the red dashed frame in Figure 7b $t = 0.6$–0.8 s, continue to move downslope under the influence of gravity, indicating the existence of a post-collision effect for basal erosion and transport.

It can also be observed that the erosion processes from the experiments are highly transient, especially with the gasified sand obscuring the captured images. Therefore, a hybrid continuum–discrete simulator is leveraged to carry out numerical back-analysis of the erosion mechanisms (to be discussed in Section 5.3).

### 4.2. Collisional Stresses Induced on the Erodible Bed

The collisional stresses induced on an erodible bed cannot be directly measured. Therefore, the collisional stresses are measured using a load plate installed on the non-erodible bed just upstream from the erodible one. It is assumed that the measured collisional stresses induced by the flow on the non-erodible bed just before the
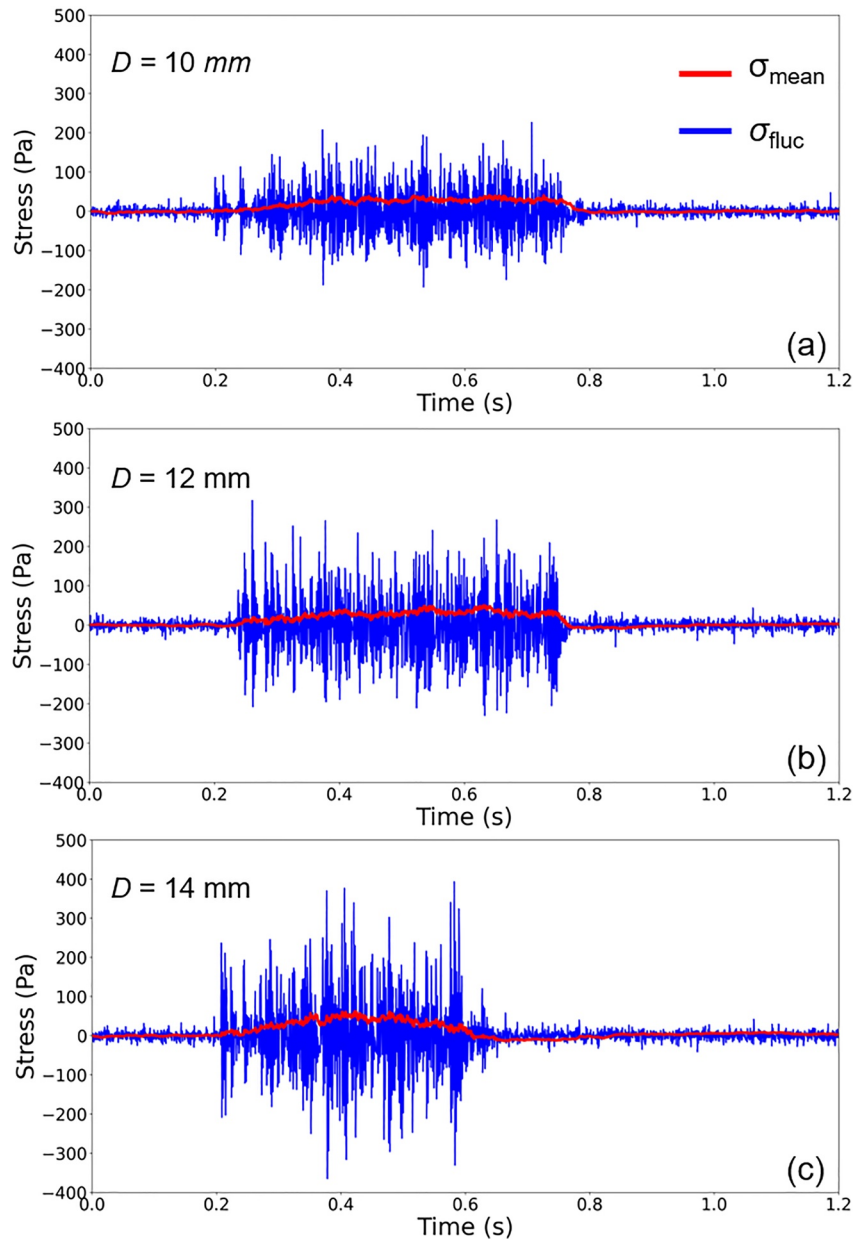
**Figure 8.** Comparison of measured collisional loads at an inclination of 30.0° with different flow particle diameters: (a) $D = 10$ mm; (b) $D = 12$ mm; and (c) $D = 14$ mm.

erodible section are representative of those induced on the erodible section. Li et al. (2022) reported that measured flow basal stress consists of two main components: the mean stress $\sigma_{mean}$, which is dependent on the flow density (Iverson et al., 2010), and the fluctuating stress $\sigma_{fluc}$, which is governed by grain-scale dynamics such as the particle diameter and velocity (McCoy et al., 2013). The mean stress and discrete collisions are represented by a smoothed profile and sharp fluctuations of the measured signals, respectively.

Figure 8 compares the measured basal stress induced by the glass bead flows with different particle diameters. We postulate that the increase in particle sizes produces less frequency and stronger collisions, making the Pareto distribution narrower. The mean stress is a moving average over a time scale of 0.02 s (Hsu et al., 2014). The fluctuation stress is calculated as $\sigma_{fluc} = \sigma - \sigma_{mean}$. It is observed that the magnitude of collisional stresses increases with particle diameter, which is consistent with the observation by Hsu et al. (2014). Furthermore, the duration and frequency of collisions become shorter as the particle size increases. This is because experiments conducted with flows consisting of larger particle diameters are fewer in number for the same comparable initial mass.
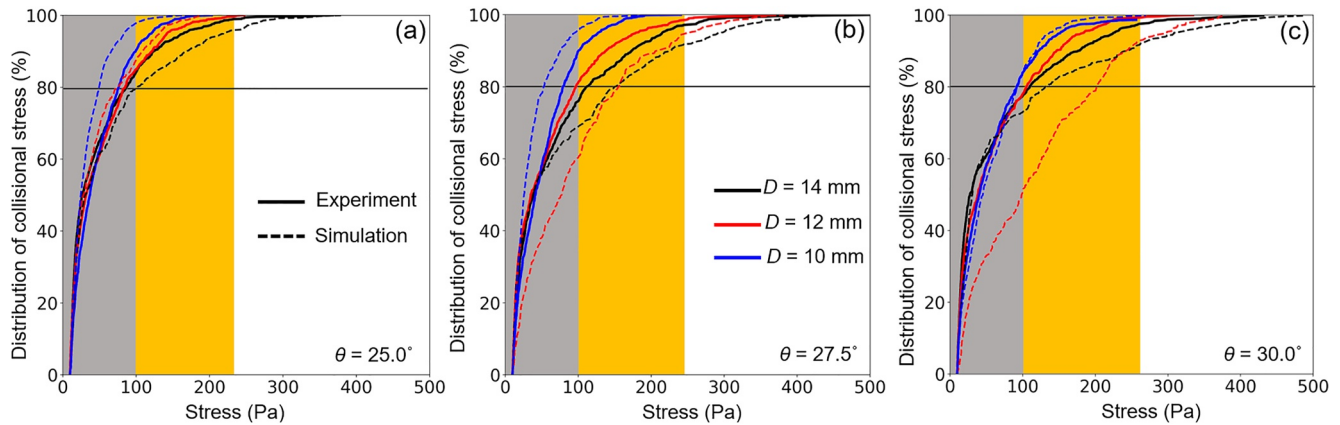
**Figure 9.** Comparison of collisional stress for different particle sizes and inclinations: (a) $\theta = 25.0°$, (b) $\theta = 27.5°$, and (c) $\theta = 30.0°$.

Evidently, the fluctuation stresses are dominant in the stress measurements. Therefore, a suitable index is needed to describe the collisional nature of the flows observed in this study. A stress-magnitude cumulative distribution (SCD) function is used to evaluate the dynamics of the discrete collisions exerted by the granular flows. The SCD function describes the distribution of collisional stresses based on their magnitudes (McCoy et al., 2013). The SCD function is also used for the calibration of the numerical input parameters of the DEM flows to simulate the collisional dynamics from the experiments.

Figure 9 shows a comparison of the measured and computed stress measurements induced by glass beads on the load plate. The solid lines show the stress cumulative distribution measured from the experiments, which is a direct rearrangement of the stress-time history in Figure 8 based on the stress magnitude and frequency. The stress = 100 Pa serves as the upper bound for the gray area, which covers 80% of the SCD for all the cases. The orange area represents stresses between 80% of the SCD lines and their reference limits, which are calculated by assuming flows are a continuum and purely frictional (Li et al., 2022).

The simulation results agree with the experimental measurement in both magnitude and distribution. However, there are notable differences for the case of $\theta = 30.0°$ and $D = 12$ mm, where the simulation results are up to 40% less than those measured. The difference can be attributed to the choice of damping coefficients for the normal and shear contact forces between discrete elements. Because a single set of damping coefficients was used for all the experimental conditions, additional damping may have been introduced for cases with high inclinations and large particle diameters.

The concentration of cumulative stresses in the region of stress >100 Pa increases with particle size (Hsu et al., 2014; Li et al., 2022) and inclination. The observed trend is because the tangential component of gravitational acceleration increases with inclination, which in turn enhances the magnitude of the collision.

The measured and computed SCD for all test configurations generally diverges in the region of stress >100 Pa (i.e., upper 20% of the distribution curve in the orange area), where higher stresses induced by larger particle diameters dominate the cumulative distribution. Nearly 80% of the collisional stresses (in the gray area) are less than 100 Pa, regardless of particle size and inclination.

The observed pattern follows the Pareto distribution—a power law probability distribution—which suggests that 80% of differences in the outcomes are due to 20% of causes. This distribution pattern was reported for studying the pattern of basal stress induced by monodispersed flows (Hsu et al., 2014; McCoy et al., 2013). In other words, the level of collisional-induced erosion and transport is dominated by the largest 20% of collisional events. The observed distribution is surprising, given the general randomness expected by discrete collisions on a soil bed. Furthermore, changes in inclination do not significantly influence the power term in the Pareto distribution function (McCoy et al., 2013).

### 4.3. Erosion Profile

Erosion is defined as the measured increase in depth compared to the initial elevation of the sand bed. More commonly, the mass of material removed is used in analytical studies to describe soil bed erosion (e.g., Pudasaini
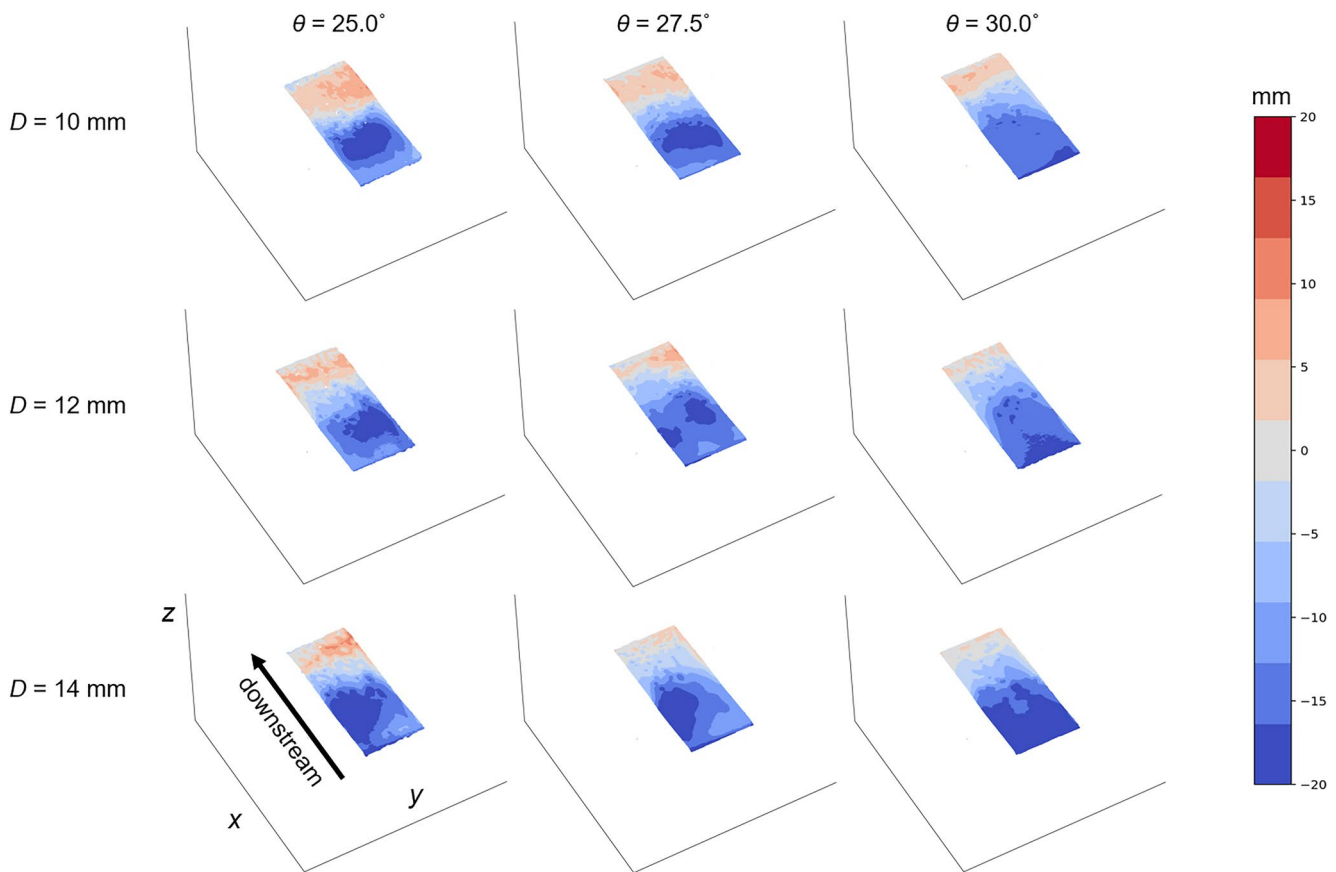
**Figure 10.** Scanned topography from each experiment.

& Krautblatter, 2021). However, the spatial variation in depth is used in this study as a direct measurement of the eroded surface from the flume experiments.

Figure 10 shows the effects of erosion and deposition on the surface profile of the erodible dry sand bed. Most erosion is observed near the interface between the non-erodible and erodible beds. Erosion gradually decreases from 20 to 0 mm downstream. Eventually, the deposition of the mobilized sand bed material causes an increase in bed depth (i.e., positive values of depth) near the end of the erodible bed section. A similar sand bed profile was reported by Song and Choi (2021) and De Haas and Woerkom (2016). The profile is caused by the sudden deceleration of the coarse grain flow due to the increased basal friction of the erodible sand bed compared to the smoother non-erodible bed. The deceleration of the glass beads is more evident with distance along the erodible bed. The deceleration of the glass beads at the flow bed interface shields the ensuing glass beads from impacting and eroding the bed (McCoy et al., 2013). Evidently, flow-bed interaction is a complex phenomenon whereby the effects of bed failure, transport, deposition, and shielding compete against each other. These mechanisms, however, are grossly simplified in the existing continuum models.

Interestingly, it can be observed that bed depth variations are not significant along the lateral direction of the channel. The boundary effect caused by the channel side walls is evidently trivial since the erosion depth only shows marginal differences smaller than 5 mm near the sidewall. This observation further supports the assumption of a projected 2D simulation along the erodible bed section. The measured results show that a small size ratio between the particle diameter and flume width selected in this study results in a relatively uniform erosion effect along the channel width. Similar observations were reported in field transport analysis for rock avalanches (Kang et al., 2017), where the surface profile of an erodible soil bed was reported to be more uniform after a rock avalanche.

The surface topography of the erodible bed indeed changes as the erosion process progresses. However, the dissipation of flow energy caused by local changes in slope on the surficial material of the erodible bed is small
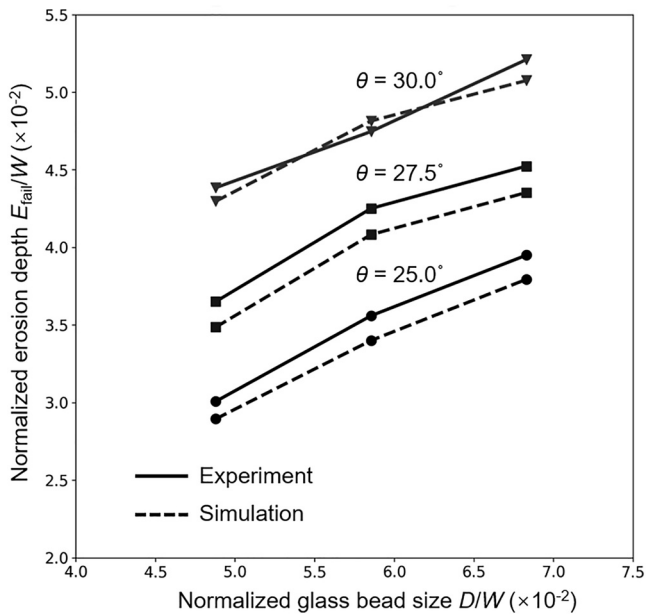
**Figure 11.** Comparison of the averaged erosion depths for different inclinations and normalized particle diameter by the channel width $W$.

compared to the overall kinetic energy of the flow resulting from the slope of the channel. For example, the total initial energy is up to 23 J, and only 2.72 J of energy is dissipated during the entire retexturing stage.

Figure 11 compares the experimental and simulation results of the normalized erosion depth $E_{fail}$, which equals the average value of $\Delta h$ normalized by the channel width. The erosion depths in the experiments are spatial averages along the erodible section measured by a scanner. Evidently, the erosion depths in the simulations match the experimental measurements well in terms of the depths and the increasing trend with particle size and inclination. This consistency validates the ability of the hybrid continuum–discrete model to simulate the erosion and transport processes of interest.

## 5. Transport Following Collision-Induced Erosion

### 5.1. Transported Mass

Figure 12 shows the equivalent transported depth of soil in the experiments and simulations. The equivalent transported depth $E_{trans}$ equals the transported soil volume divided by the surface area of the erodible soil bed. Generally, it can be observed that the transported mass increases with inclination and particle size. However, unlike the measured erosion depths, a slight increase in transported mass with particle size is not observed for $\theta = 30°$. Larger diameter glass bead flows (i.e., $D = 12$ mm and $D = 14$ mm) result in less bed material transport than those caused by smaller glass bead flow (i.e.,

$D = 10$ mm). This is because sand inclined near its angle of repose (i.e., 32°) is metastable. Therefore, the collisional stresses induced by the glass beads easily mobilize the sand bed material. So direct collisions between the glass beads and soil bed material are not the only factors driving the transport. The influence of particle size on transport becomes less obvious when the basal material is metastable.

It can also be observed that the transported depths in the simulations agree well with the experimental data. In particular, the results of transported depth near the repose angle of $\theta = 32°$ are successfully captured. Results indicate that a metastable sand bed material can influence the transport process during collisions between coarse grains in granular flows. In general, the validation of transported mass ensures that the simulations in this study are reliable.
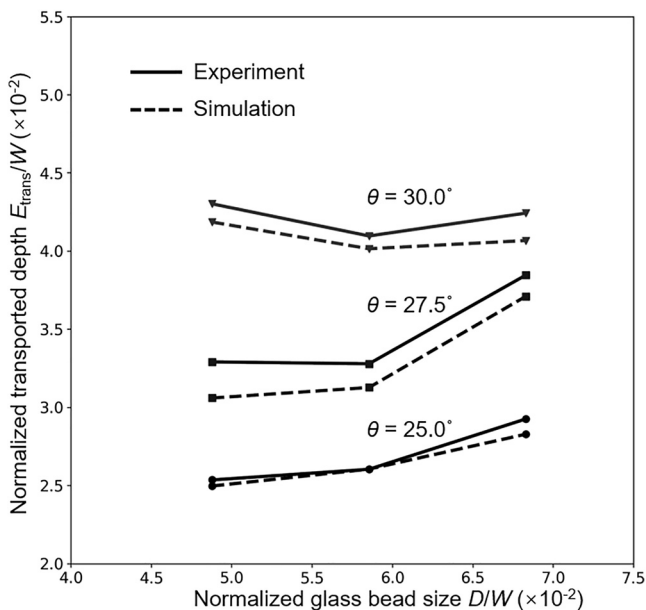
### 5.2. Quantitative Relationships Between Bed Erosion and Transport

The relationship between the erosion $E_{fail}$ and transport $E_{trans}$ depths may be used to demonstrate the importance of differentiating between failed and transported bed volumes. The equivalent transport depth should be larger than the transport depth since not all basal material sheared to failure by collisions is incorporated into the collisional glass bead flows owing to their limited transport capacity. Quantitative verification of such a relationship helps to confirm the mechanical differences between erosion and transport and evaluate the transport capacity of collisional coarse grain flows. Figure 13 shows that all test results satisfy the relationship of $E_{fail} > E_{trans}$ because all data points are above the reference line of $E_{fail} = E_{trans}$.

The condition of $E_{fail} = E_{trans}$ is the theoretical limit whereby the eroded and transported materials are the same. Such an assumption is often adopted by computational frameworks based on the theory of friction-induced erosion (Medina et al., 2008; Pudasaini & Krautblatter, 2021), which assumes that flows transport all basal materials that are sheared to failure by the frictional stress due to the downstream momentum conservation.

However, the experimental results in this study indicate that the basal materials that are eroded by collisional stresses are not entirely transported by the
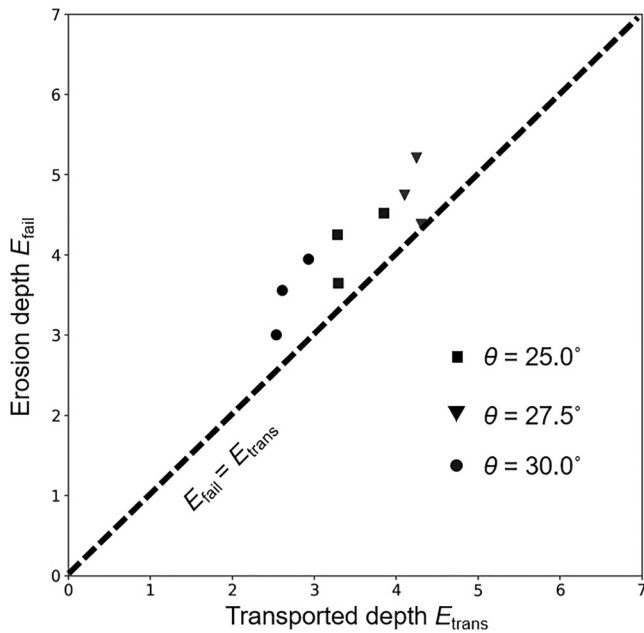


**Figure 12.** Comparison of equivalent transported depths for different normalized particle diameters by channel width $W$, and inclination.

**Figure 13.** Relationship between the bed failure depth $E_{fail}$ and equivalent transport depth $E_{trans}$.

flows. This is because the stress is applied to the soil through the impacts of glass beads. In this way, the flow momentum is largely dissipated through the plastic deformation during the impacts between glass beads and sand, which limits the capacity of collisional flows to move the failed sand downstream.

Based on the results of this study, it is evident that an overestimation of transportation, or underestimation of basal erosion, occurs if $E_{fail} = E_{trans}$ is used for predictions. So, if bed erosion and transport are not distinguished, then the volume of bed material enriched in the flow and final deposition volumes are likely to be overestimated. This effect may compound with chainage and affect the accuracy of hazard assessments (i.e., runout distance).

### 5.3. Mechanisms of Collision-Induced Erosion and Transport

The numerical simulations are leveraged to elucidate the driving mechanisms of collisional-induced erosion and transport. The snapshots of the simulations identify three stages for erosion and transport by collisional flows: (a) surface retexturing, (b) plowing, and (c) bed mobilization. In Figures 13–15, the three stages are demonstrated by the simulation results when $D = 14$ mm and $\theta = 30.0°$.

Figure 14 shows the surface retexturing stage. Similar to the experimental results, the simulation results involve a mild interaction between the glass beads and the soil bed, as highlighted in the dashed boxes in Figures 14b and 14c. The simulation results show that the first glass bead skims over the sand bed and creates a protrusion. When traced in the simulation, the protrusion becomes impacted by an ensuing glass bead. Observations suggest that at the initial stage, collision-induced transport is enhanced with an increasing number of impacts. Consequently, the surface profile of the bed becomes increasingly irregular. Although the levels of shear failure and transport are relatively small, the retexturing of the bed surface profile is essential for the second stage of flow-bed interaction.

Figure 15 demonstrates the plowing stage, where the bed material is transported through the direct collisions between the glass beads and protrusions on the soil bed. Increasing transport occurs as glass beads interact with the bed, which agrees with experimental observations. Owing to surface retexturing, the number of protrusions and undulations increases, enhancing collisions with the ensuing glass beads of the flow. The collisions between glass beads and protrusions mobilize the sand bed material via plowing and gasification downstream.

Meanwhile, based on the experimental (Section 4.1) and simulation (Section 5.3) results, local changes to the surface of the erodible bed (i.e., slope) are described as surface retexturing in Figure 14 and plowing in Figure 15.
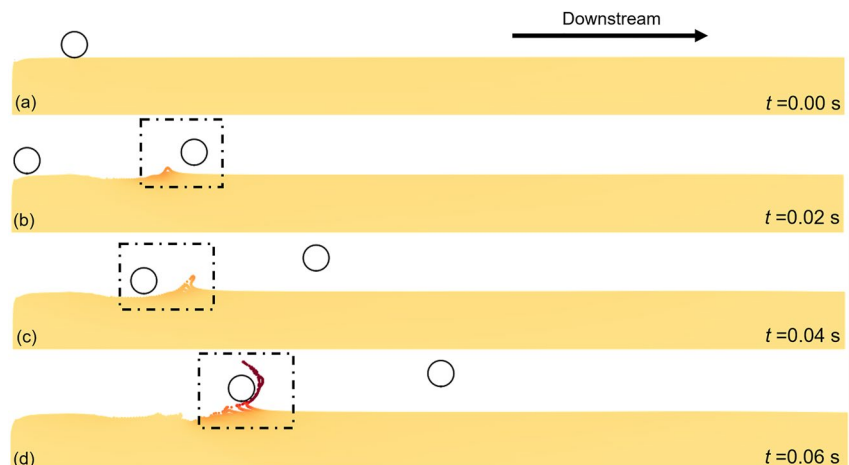


**Figure 14.** Surface retexturing stage in the simulation case of $D = 14$ mm and $\theta = 30.0°$. (a) $t = 0.00$ s, (b) $t = 0.02$ s, (c) $t = 0.04$ s, (d) $t = 0.06$ s. The colorbar represents the velocity (m/s) in the downstream direction.
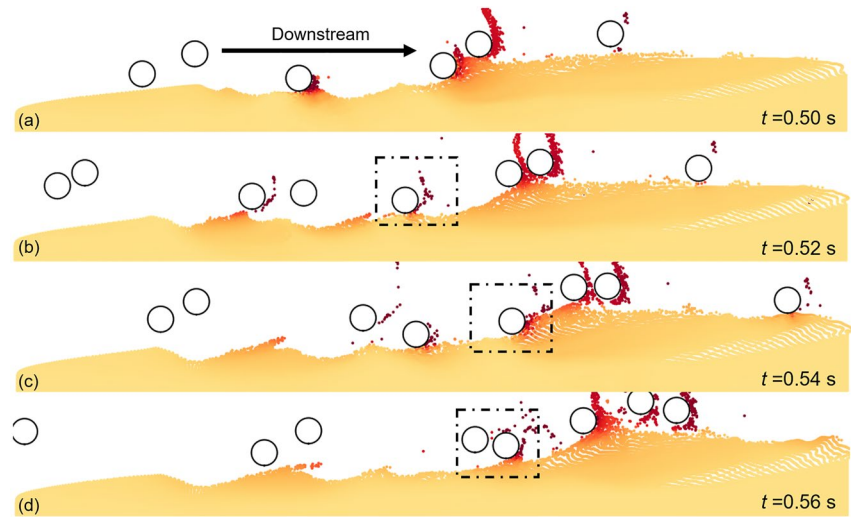
**Figure 15.** Plowing stage in the simulation case of $D = 14$ mm and $\theta = 30.0°$. (a) $t = 0.50$ s, (b) $t = 0.52$ s, (c) $t = 0.54$ s, and (d) $t = 0.56$ s. The colorbar represents the velocity (m/s) in the downstream direction.

The erodible bed surface first becomes irregular with protrusions at the retexturing stage under the influence of particle collisions. The protrusions further enhance collisions with the ensuing glass beads of the flow, allowing the particles to plow the bed materials. Therefore, the topographical changes of the erodible bed are merely protrusions (i.e., local changes in slope) that partially drive the erosion and transport processes.

Figure 16 shows the bed mobilization stage, where the bed material moves without directly relating to glass bead collisions. It can be observed in the dashed frame of Figure 16 that there are areas where nearly no glass beads directly impact it. Yet, the bed material still flows downstream with a non-trivial velocity of up to $v_x = 0.5$ m/s because previous impacts have mobilized it. Findings help to explain why the erosion depth is deepest near the interface between the erodible and non-erodible beds, yet none of the glass beads were deposited there.

## 6. Discussions

This study provides new insights into the mechanisms of erosion and transport of soil bed material by collisional granular flow fronts. A debris flow front is typically enriched with coarse grains and poorly saturated
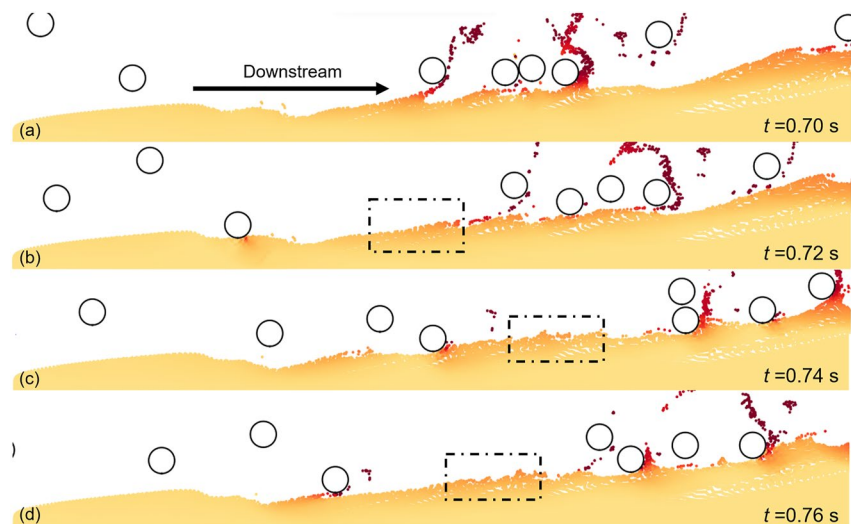


**Figure 16.** Bed mobilization stage in the simulation case of $D = 14$ mm and $\theta = 30°$. (a) $t = 0.70$ s, (b) $t = 0.72$ s, (c) $t = 0.74$ s, and (d) $t = 0.76$ s. The colorbar represents the velocity (m/s) in the downstream direction.

(Iverson, 1997). As a result, collisional stresses are dominant at the flow front. Based on field monitoring, McArdell et al. (2007) reported that coarse particles at a debris flow front do not exhibit enduring contact with each other. Therefore, the effects of fluid and frictional stress are diminished, and dry collisional coarse-grained granular flows are used to model prototype flow fronts in this study. It is acknowledged, however, that the stresses within debris flow are more complicated than model flows due to the polydispersed nature of particles and the presence of a viscous interstitial fluid (De Haas & Woerkom, 2016; Roelofs et al., 2022; Schürch et al., 2011). More specifically, for field flows, solid stresses (i.e., frictional shear stress and collisional stresses) are responsible for soil bed erosion at the poorly saturated boulder-enriched debris flow front. In contrast, the fluid stress (i.e., hydrodynamic shear stress) dominates the soil bed erosion at the liquefied body and tail of the debris flow. Therefore, further research is encouraged to investigate the influence of the spatiotemporal effects of mesoscopic stresses on soil bed erosion and transport.

### 6.1. Flow Properties

The grain diameter and size distribution of particles comprising a flow influence the relative contributions from frictional and collision grain stresses (Farin et al., 2019). Specifically, with an increase in particle size, a granular geophysical flow that behaves like a frictional continuum may gradually become discrete and collisional, leading to changes in the erosion dynamics and transported volumes (Farin et al., 2019; Schürch et al., 2011). Studies on the size effect (De Haas & Woerkom, 2016) have demonstrated the competing effects between the collisional and frictional-induced transport, considering a flow consisting of a frictional body with a collisional front. Typically, well-graded flow mixtures may behave less collisional and exert more shear forces when eroding basal materials (Roelofs et al., 2022). Therefore, further studies using a wider distribution of grain sizes based on our experimental and numerical setting can further shed light on the transition between frictional and collisional erosion and transport.

The flow discharge is another important factor strongly correlated with the erosion and transport capacities of granular flows. Specifically, the increase in flow discharge can further enhance erosion (De Haas & Woerkom, 2016; Schürch et al., 2011) due to increased flow inertia. However, the quantitative relationship between discharge and transport capacity is non-monotonic, which depends on the relative velocities of erosion and transport (Pudasaini & Krautblatter, 2021). Therefore, the correlation between collisional stress and flow discharge requires further investigation.

### 6.2. Bed Properties and Signal

This study investigates the erosion of a dry sandy bed by dry coarse-grained granular flows dominated by collisional stresses. It is acknowledged that the bed condition (i.e., dry) and flows modeled in this study represent simplified conditions compared to those in the field. In the field, the water content of soil beds varies over a broad range (De Haas et al., 2022; McCoy et al., 2013), and stresses within a debris flow are more complex owing to heterogeneity and the presence of a pore fluid (De Haas & Woerkom, 2016; Roelofs et al., 2022; Schürch et al., 2011). Soil with different water content exhibits different mechanical responses when sheared (Fredlund et al., 1996). Specifically, soil strength exhibits a parabolic relationship with soil water content (Fredlund et al., 1996). Consequently, soil bed erosion and transport exhibit a parabolic relationship with soil water content (Song & Choi, 2021). Furthermore, the solid stresses (i.e., frictional and collisional shear stresses) drive soil bed erosion at the poorly saturated coarse-enriched debris flow front (Iverson, 1997). In contrast, fluid stresses (i.e., hydrodynamic shear stress) drive soil bed erosion at the liquefied body and tail of a debris flow (Berger et al., 2011; McCoy et al., 2013). Therefore, investigations on the competing effects of flow stresses on soil bed erosion are warranted.

The use of uniform dry sand may also play a role in the observed erosion mechanisms. Different erosion mechanisms may be observed if bed materials contain larger grains (Stock & Dietrich, 2003; Turowski & Cook, 2017). The large grains may limit erosion owing to their large inertia and change the erosion pattern (De Haas & Woerkom, 2016).

Furthermore, existing research has shed light on the real-time analysis of the debris flow stresses through monitoring the seismic signal generated by the debris flow (De Haas et al., 2021; Farin et al., 2019; Zhang et al., 2021a, 2021b). Further research can be conducted to investigate the prediction of soil bed erosion and debris-flow volume from the real-time monitored seismic signal.

### 6.3. Stress Measurement and Cumulative Distribution

There is no feasible approach to directly measure the collisional stress induced on the erodible sand bed in the experiments. So, measurements from the force plate on the rigid bed before the erodible one are used to calibrate the numerical solver to ensure that similar granular collisional dynamics are simulated. Interestingly, it can be observed that the Pareto distribution holds true regardless of the basal condition because it is physically generated from self-organized criticality (Newman, 2005), which is a self-organizing pattern of inter-particle collisions in coarse-grained flows. Also, field observation data reported by McCoy et al. (2013) confirm the Pareto distribution of collisional stress under various basal conditions (i.e., even for more complex field conditions).

In addition, the role that Pareto distribution played in collisional erosion deserves special attention. This pattern of collisional force in coarse particle flows hints at a profound physical phenomenon that brews measurable certainness in a seemingly random process of coarse grain collisions (Newman, 2005). The Pareto distribution stands regardless of the basal condition. Because it is physically generated from the self-organized criticality (Newman, 2005)—a self-organizing pattern of the inter-particle collisions in coarse-grained flows. For analytical and numerical models, the observed Pareto distribution pattern provides a potential opportunity for incorporating collisional erosion and transport into continuum-based models, if the SCD based on the Pareto distribution can be estimated based on the flow dynamics and particle sizes (Hsu et al., 2014). The study may benefit hazard assessments that consider geophysical flow erosion and transport. Also, the Pareto distribution reported in this study can significantly benefit the existing studies relating seismic signals with debris flow characteristics (De Haas et al., 2021; Farin et al., 2019). Our results support a standard distribution to analytically represent collisional stresses caused by large particles in debris flows. It allows convenient incorporation of the particle size effect into the existing frameworks to retrieve flow characteristics based on seismic signal features (Zhang et al., 2021a, 2021b).

## 7. Summary and Conclusions

This work has investigated the erosion and transport mechanisms of dry soil beds induced by collisional and coarse grain flows. A series of flume experiments were carried out and then back-analyzed through hybrid continuum–discrete simulations. New insights gained from the combined experimental and numerical investigation may be summarized as follows:

1. The collisional stresses of glass beads roughen the soil bed surface. The irregular surface topography facilitates increased collision frequency, which in turn enhances bed failure and transport. Although the topography of soil beds is not currently considered in hazard assessment tools, findings suggest that the bed topography and morphology have profound effects on erosion processes.
2. Collisions can more easily destabilize soil beds inclined near their angle of repose. Erosion and transport may significantly increase with even a subtle change in the inclination. Such scenarios deserve attention when carrying out hazard assessments of the mobility of a granular flow or in the prediction of the design volume required for protection structures.
3. Contrary to the existing models that are based on continuum-based frictional induced erosion, results from this study show that eroded basal materials are not entirely transported by collisional granular geophysical flow. Findings suggest that improved hazard assessments require erosion and transport to be differentiated to avoid a potential overestimation of the final volume of soil transported.
4. The collisional stresses of the monodisperse flows in this study follow the Pareto distribution—a power law probability distribution—which suggests that 80% of differences in the outcomes are due to 20% of causes. This pattern of collisional force in coarse particle flows suggests that there is measurable certainness in a seemingly random process of coarse grain collisions with an erodible sand bed.

## Data Availability Statement

The experimental data sets and code for simulation can be accessed through the Digital repository of The University of Hong Kong, which is open for public access and download (Jiang et al., 2023): https://doi.org/10.25442/hku.23612253. The data for plotting the particle size distribution of Toyoura sand can be found in Dong et al. (2016): https://doi.org/10.1061/(ASCE)GM.1943-5622.0000524. The data processing was conducted using Python Language Reference, version 3.9, available at http://www.python.org, Python Software Foundation (2020).

## References

Agarwal, S., Karsai, A., Goldman, D. I., & Kamrin, K. (2021). Surprising simplicity in the modeling of dynamic granular intrusion. *Science Advances*, *7*(17), eabe0631. https://doi.org/10.1126/sciadv.abe0631

Bagnold, R. A. (1954). Experiments on a gravity-free dispersion of large solid spheres in a Newtonian fluid under shear. *Proceedings of the Royal Society of London. Series A. Mathematical and Physical Sciences*, *225*(1160), 49–63.

Berger, C., McArdell, B. W., & Schlunegger, F. (2011). Direct measurement of channel erosion by debris flows, Illgraben, Switzerland. *Journal of Geophysical Research*, *116*(F1), F01002. https://doi.org/10.1029/2010jf001722

Brackbill, J. U., & Ruppel, H. M. (1986). FLIP: A method for adaptively zoned, particle-in-cell calculations of fluid flows in two dimensions. *Journal of Computational Physics*, *65*(2), 314–343. https://doi.org/10.1016/0021-9991(86)90211-1

Cagnoli, B., & Piersanti, A. (2015). Grain size and flow volume effects on granular flow mobility in numerical simulations: 3-D discrete element modeling of flows of angular rock fragments. *Journal of Geophysical Research: Solid Earth*, *120*(4), 2350–2366. https://doi.org/10.1002/2014jb011729

Cao, Z., Pender, G., Wallis, S., & Carling, P. (2004). Computational dam-break hydraulics over erodible sediment bed. *Journal of Hydraulic Engineering*, *130*(7), 689–703. https://doi.org/10.1061/(asce)0733-9429(2004)130:7(689)

Choi, C. E., & Song, P. (2023). New unsaturated erosion model for landslide: Effects of flow particle size and debunking the importance of frictional stress. *Engineering Geology*, *315*, 107024. https://doi.org/10.1016/j.enggeo.2023.107024

Cui, M., Chen, F., & Bu, F. (2021). Multiphase theory of granular media and particle simulation method for projectile penetration in sand beds. *International Journal of Impact Engineering*, *157*, 103962. https://doi.org/10.1016/j.ijimpeng.2021.103962

Cui, Y., Cheng, D., Choi, C., Jin, W., Lei, Y., & Kargel, J. (2019). The cost of rapid and haphazard urbanization: Lessons learned from the Freetown landslide disaster. *Landslides*, *16*(6), 1167–1176. https://doi.org/10.1007/s10346-019-01167-x

Cundall, P. A., & Strack, O. D. L. (1979). Discrete numerical model for granular assemblies. *Géotechnique*, *29*(1), 47–65. https://doi.org/10.1680/geot.1979.29.1.47

De Haas, T., Åberg, A. S., Walter, F., & Zhang, Z. (2021). Deciphering seismic and normal-force fluctuation signatures of debris flows: An experimental assessment of effects of flow composition and dynamics. *Earth Surface Processes and Landforms*, *46*(11), 2195–2210. https://doi.org/10.1002/esp.5168

De Haas, T., McArdell, B. W., Nijland, W., Åberg, A. S., Hirschberg, J., & Huguenin, P. (2022). Flow and bed conditions jointly control debris-flow erosion and bulking. *Geophysical Research Letters*, *49*(10), e2021GL097611. https://doi.org/10.1029/2021gl097611

De Haas, T. D., & Woerkom, T. V. (2016). Bed scour by debris flows: Experimental investigation of effects of debris-flow composition. *Earth Surface Processes and Landforms*, *41*(13), 1951–1966. https://doi.org/10.1002/esp.3963

DEM Solutions. (2014). EDEM 2.6 theory reference guide.

Dong, Q., Xu, C., Cai, Y., Juang, H., Wang, J., Yang, Z., & Gu, C. (2016). Drained instability in loose granular material [Dataset]. International Journal of Geomechanics, *16*(2), 04015043. https://doi.org/10.1061/(ASCE)GM.1943-5622.0000524

Drucker, D. C., & Prager, W. (1952). Soil mechanics and plastic analysis or limit design. *Quarterly of Applied Mathematics*, *10*(2), 157–165. https://doi.org/10.1090/qam/48291

Dunatunga, S., & Kamrin, K. (2015). Continuum modelling and simulation of granular flows through their many phases. *Journal of Fluid Mechanics*, *779*, 483–513. https://doi.org/10.1017/jfm.2015.383

Dunatunga, S., & Kamrin, K. (2017). Continuum modeling of projectile impact and penetration in dry granular media. *Journal of the Mechanics and Physics of Solids*, *100*, 45–60. https://doi.org/10.1016/j.jmps.2016.12.002

Farin, M., Tsai, V. C., Lamb, M. P., & Allstadt, K. E. (2019). A physical model of the high-frequency seismic signal generated by debris flows. *Earth Surface Processes and Landforms*, *44*(13), 2529–2543. https://doi.org/10.1002/esp.4677

Fei, Y., Guo, Q., Wu, R., Huang, L., & Gao, M. (2021). Revisiting integration in the material point method: A scheme for easier separation and less dissipation. *ACM Transactions on Graphics*, *40*(4), 1–16. https://doi.org/10.1145/3450626.3459678

Fredlund, D. G., Xing, A., Fredlund, M. D., & Barbour, S. L. (1996). The relationship of the unsaturated soil shear strength to the soil-water characteristic curve. *Canadian Geotechnical Journal*, *33*(3), 440–448. https://doi.org/10.1139/t96-065

Harlow, F. H. (1964). The particle-in-cell computing method for fluid dynamics. *Methods in Computational Physics*, *3*, 319–529.

Hsu, L., Dietrich, W. E., & Sklar, L. S. (2014). Mean and fluctuating basal forces generated by granular flows: Laboratory observations in a large vertically rotating drum. *Journal of Geophysical Research: Earth Surface*, *119*(6), 1283–1309. https://doi.org/10.1002/2013jf003078

Hungr, O., McDougall, S., & Bovis, M. (2005). *Debris-flow hazards and related phenomena*. Springer.

Iverson, R. M. (1997). The physics of debris flows. *Reviews of Geophysics*, *35*(3), 245–296. https://doi.org/10.1029/97rg00426

Iverson, R. M. (2012). Elementary theory of bed-sediment entrainment by debris flows and avalanches. *Journal of Geophysical Research*, *117*(F3), F03006. https://doi.org/10.1029/2011jf002189

Iverson, R. M. (2015). Scaling and design of landslide and debris-flow experiments. *Geomorphology*, *244*, 9–20. https://doi.org/10.1016/j.geomorph.2015.02.033

Iverson, R. M., Logan, M., LaHusen, R., & Berti, M. (2010). The perfect debris flow? Aggregated results from 28 large-scale experiments. *Journal of Geophysical Research*, *115*(F3), F03005. https://doi.org/10.1029/2009jf001514

Iverson, R. M., Reid, M. E., Logan, M., Lahusen, R. G., Godt, J. W., & Griswold, J. P. (2011). Positive feedback and momentum growth during debris-flow entrainment of wet bed sediment. *Nature Geoscience*, *4*(2), 116–121. https://doi.org/10.1038/ngeo1040

Jakob, M., & Friele, P. (2009). Frequency and magnitude of debris flows on Cheekye River, British Columbia. *Geomorphology*, *114*(3), 382–395. https://doi.org/10.1016/j.geomorph.2009.08.013

Jiang, Y., Li, M., Jiang, C., & Alonso-Marroquin, F. (2020). A hybrid material-point spheropolygon-element method for solid and granular material interaction. *International Journal for Numerical Methods in Engineering*, *121*(14), 3021–3047. https://doi.org/10.1002/nme.6345

Jiang, Y., Song, P., Choi, C. E., & Choo, J. (2023). Erosion and transport of dry soil bed by collisional granular flow. (Version one) [Dataset] & [Software]. HKUL Digital Repository. https://doi.org/10.25442/hku.23612253

Jiang, Y., Zhao, Y., Choi, C. E., & Choo, J. (2022). Hybrid continuum–discrete simulation of granular impact dynamics. *Acta Geotechnica*, *17*(12), 5597–5612. https://doi.org/10.1007/s11440-022-01598-2

Kang, C., Chan, D., Su, F., & Cui, P. (2017). Runout and entrainment analysis of an extremely large rock avalanche—A case study of Yigong, Tibet, China. *Landslides*, *14*(1), 123–139. https://doi.org/10.1007/s10346-016-0677-7

Lade, P. V. (2010). The mechanics of surficial failure in soil slopes. *Engineering Geology*, *114*(1–2), 57–64. https://doi.org/10.1016/j.enggeo.2010.04.003

Lagioia, R., Sanzeni, A., & Colleselli, F. (2006). Air, water and vacuum pluviation of sand specimens for the triaxial apparatus. *Soils and Foundations*, *46*(1), 61–67. https://doi.org/10.3208/sandf.46.61

Li, K., Wang, Y., Cheng, Q., Lin, Q., Wu, Y., & Long, Y. (2022). Insight into granular flow dynamics relying on basal stress measurements: From experimental flume tests. *Journal of Geophysical Research: Solid Earth*, *127*(3), e2021JB022905. https://doi.org/10.1029/2021jb022905

Li, M., He, Y., Liu, W., Liu, Y., Huang, C., & Jiang, R. (2020). Effect of adding finer particles on the transport characteristics of coarse-particle slurries in pipelines. *Ocean Engineering*, *218*, 108160. https://doi.org/10.1016/j.oceaneng.2020.108160

Li, M., Kaufman, D. M., & Jiang, C. (2021). Codimensional incremental potential contact. *ACM Transactions on Graphics*, *40*(4–170), 1–24. https://doi.org/10.1145/3476576.3476756

McArdell, B. W., Bartelt, P., & Kowalski, J. (2007). Field observations of basal forces and fluid pore pressure in a debris flow. *Geophysical Research Letters*, *34*(7), L07406. https://doi.org/10.1029/2006gl029183

McCoy, S. W., Tucker, G. E., Kean, J. W., & Coe, J. A. (2013). Field measurement of basal forces generated by erosive debris flows. *Journal of Geophysical Research: Earth Surface*, *118*(2), 589–602. https://doi.org/10.1002/jgrf.20041

McDougall, S., & Hungr, O. (2005). Dynamic modeling of entrainment in rapid landslides. *Canadian Geotechnical Journal*, *42*(5), 1437–1448. https://doi.org/10.1139/t05-064

Medina, V., Hürlimann, M., & Bateman, A. (2008). Application of FLATModel, a 2D finite volume code, to debris flows in the northeastern part of the Iberian Peninsula. *Landslides*, *5*(1), 127–142. https://doi.org/10.1007/s10346-007-0102-3

Mirghasemi, A. A., Rothenburg, L., & Matyas, E. L. (2002). Influence of particle shape on engineering properties of assemblies of two-dimensional polygon-shaped particles. *Géotechnique*, *52*(3), 209–217. https://doi.org/10.1680/geot.2002.52.3.209

Nadimi, S., Otsubo, M., Fonseca, J., & Sullivan, C. O. (2019). Numerical modelling of rough particle contacts subject to normal and tangential loading. *Granular Matter*, *21*(108), 108. https://doi.org/10.1007/s10035-019-0970-y

Newman, M. E. J. (2005). Power laws, Pareto distributions and Zipf's law. *Contemporary Physics*, *46*(5), 323–351. https://doi.org/10.1080/00107510500052444

Pasqua, A., Leonardi, A., & Pirulli, M. (2022). Coupling Depth-Averaged and 3D numerical models for the simulation of granular flows. *Computers and Geotechnics*, *149*, 104879. https://doi.org/10.1016/j.compgeo.2022.104879

Pudasaini, S. P., & Krautblatter, M. (2021). The mechanics of landslide mobility with erosion. *Nature Communications*, *12*(6793), 1–15. https://doi.org/10.1038/s41467-021-26959-5

Python Software Foundation. (2020). Python Language Reference, version 3.9 [Software]. Retrieved from http://www.python.org

Roelofs, L., Colucci, P., & de Haas, T. (2022). How debris-flow composition affects bed erosion quantity and mechanisms: An experimental assessment. *Earth Surface Processes and Landforms*, *47*(8), 2151–2169. https://doi.org/10.1002/esp.5369

Savage, S. B., & Hutter, K. (1989). The motion of a finite mass of granular material down a rough incline. *Journal of Fluid Mechanics*, *199*, 177–215. https://doi.org/10.1017/s0022112089000340

Schofield, A. N. (2006). Interlocking, and peak and design strengths. *Géotechnique*, *56*(5), 357–358. https://doi.org/10.1680/geot.2006.56.5.357

Schürch, P., Densmore, A. L., Rosser, N. J., & McArdell, B. W. (2011). Dynamic controls on erosion and deposition on debris-flow fans. *Geology*, *39*(9), 827–830. https://doi.org/10.1130/g32103.1

Song, P. J., & Choi, E. C. (2021). Revealing the importance of capillary and collisional stresses on soil bed erosion induced by debris flows. *Journal of Geophysical Research: Earth Surface*, *126*(5), 1–16. https://doi.org/10.1029/2020jf005930

Sovilla, B., Burlando, P., & Bartelt, P. (2006). Field experiments and numerical modeling of mass entrainment in snow avalanches. *Journal of Geophysical Research*, *111*(F3), F03007. https://doi.org/10.1029/2005jf000391

Stock, J., & Dietrich, W. E. (2003). Valley incision by debris flows: Evidence of a topographic signature. *Water Resources Research*, *39*(4), 1089. https://doi.org/10.1029/2001wr001057

Turowski, J. M., & Cook, K. L. (2017). Field techniques for measuring bedrock erosion and denudation. *Earth Surface Processes and Landforms*, *42*(1), 109–127. https://doi.org/10.1002/esp.4007

Zhang, Z., Walter, F., McArdell, B. W., de Haas, T., Wenner, M., Chmiel, M., & He, S. (2021a). Analyzing bulk flow characteristics of debris flows using their high frequency seismic signature. *Journal of Geophysical Research: Solid Earth*, *126*(12), e2021JB022755. https://doi.org/10.1029/2021jb022755

Zhang, Z., Walter, F., McArdell, B. W., Wenner, M., Chmiel, M., de Haas, T., & He, S. (2021b). Insights from the particle impact model into the high-frequency seismic signature of debris flows. *Geophysical Research Letters*, *48*(1), e2020GL088994. https://doi.org/10.1029/2020gl088994

Zhao, Y., & Choo, J. (2020). Stabilized material point methods for coupled large deformation and fluid flow in porous materials. *Computer Methods in Applied Mechanics and Engineering*, *362*, 112742. https://doi.org/10.1016/j.cma.2019.112742

Zhao, Y., Choo, J., Jiang, Y., & Li, L. (2023). Coupled material point and level set methods for simulating soils interacting with rigid objects with complex geometry. *Computers and Geotechnics*, *163*, 105708. https://doi.org/10.1016/j.compgeo.2023.105708

Zhao, Y., Choo, J., Jiang, Y., Li, M., Jiang, C., & Soga, K. (2022). A barrier method for frictional contact on embedded interfaces. *Computer Methods in Applied Mechanics and Engineering*, *393*, 114820. https://doi.org/10.1016/j.cma.2022.114820

Zhou, G. G., Cui, K. F., Jing, L., Zhao, T., Song, D., & Huang, Y. (2020). Particle size segregation in granular mass flows with different ambient fluids. *Journal of Geophysical Research: Solid Earth*, *125*(10), e2020JB019536. https://doi.org/10.1029/2020jb019536

## Erratum

In the originally published version of this article, the authors Pengjia Song and Clarence E. Choi were incorrectly affiliated to both the Institut für Baumechanik und Numeriche Mechanik, Leibniz Universität Hannover, Hannover, Germany, and the Department of Civil Engineering, the University of Hong Kong, Hong Kong, China. The correct affiliation for both authors should be only the Department of Civil Engineering, the University of Hong Kong, Hong Kong, China. The errors have been corrected, and this may be considered the authoritative version of record.